ADVANCED MATERIALS
www.advmat.de

Electrically Generated Exciton Polaritons with Spin On-Demand

*Yutao Wang, Giorgio Adamo, Son Tung Ha, Jingyi Tian, and Cesare Soci**

Generation and manipulation of exciton polaritons with controllable spin could deeply impact spintronic applications, quantum simulations, and quantum information processing, but is inherently challenging due to the charge neutrality of the polariton and the device complexity it requires. Here, electrical generation of spin-polarized exciton polaritons in a monolithic dielectric perovskite metasurface embedded in a light-emitting transistor is demonstrated. A finely tailored interplay of in- and out-of-plane symmetry breaking of the metasurface allows to lift the spin degeneracy through the polaritonic Rashba effect, yielding high spin purity with normalized Stokes parameter of $S_3 \approx 0.8$. Leveraging on spin-momentum locking, the unique *metatransistor* device architecture enables electrical control of spin and directionality of the polaritonic emission. Here, the development of compact and tunable spintronic devices is advanced and an important step toward the realization of electrically pumped inversionless spin-lasers is represented.

1. Introduction

Exciton-polaritons are hybrid quasiparticles of bosonic nature which emerge from the strong coupling between confined electromagnetic modes and electron–hole bound states in condensed matter. As such, the properties they inherit from their photonic and electronic constituents, that is small effective mass, strong nonlinearities and fast relaxation,[1–9] make them an exciting platform for fundamental studies of Bose-Einstein condensation,[1,3,10] superfluidity,[5,11] and for the realization of classical[12–14] and quantum optoelectronic devices.[15] Imparting an additional spin degree of freedom to the polaritons, either through the electronic or the photonic spin, can open new avenues for spintronic applications: the ability to efficiently create highly pure spin-polariton states, to electrically generate them, and to dynamically manipulate spin selectivity and directionality, without the need of external optical components, would have a vast impact for the realization of functional optospintronic devices,[16–19] quantum information processors,[15] and neuromorphic computers.[8] However, the realization of electrically driven spin-polarized polariton devices has been hindered so far by the inherent charge neutrality of the polaritons and the complex device architectures needed to control the polariton spin.

Due to their bosonic nature, the spin of polaritons can be described by an integer number ($\sigma = \pm 1$). The creation of a spin-polarized polaritonic states requires lifting the spin degeneracy. While this is attainable by using magnetic fields to break time-reversal symmetry,[20–22] magnetism-free methods for producing spin-polarized polaritons are actively researched. One possibility is to use excitonic materials with broken inversion symmetry in their electronic transitions embedded in microcavities.[23–26] A more flexible approach, unbound by the electronic spin properties of the material, is to introduce spin–orbit coupling in photonic microcavities.[17–19,27,28] This approach has led to fascinating implementations of polaritonic topological insulators,[28] synthetic gauge fields,[27] and polaritonic spin Hall effects.[17]

Recently, photonic bound states in the continuum (BIC)-modes that remain localized in spite of existing in a continuous spectrum of radiating waves,[29,30] have been used to realize perfectly confined states with theoretically infinite-Q resonances, facilitating strong light–matter interaction.[10,31–34] Γ-BIC, which are protected by the symmetry mismatch between the photonic mode profiles and the out-of-plane propagating waves, manifest as polarization singularities (V-points) at the center of the Brillouin zone. Due to the spin–orbit coupling, Γ-BIC can be evolved into off-Γ, purely circularly polarized states (C-points) by breaking the in-plane inversion symmetry of the photonic cavity

---

Y. Wang, G. Adamo, J. Tian[+], C. Soci
Centre for Disruptive Photonic Technologies, TPI
Nanyang Technological University
21 Nanyang Link, Singapore 637371, Singapore
E-mail: csoci@ntu.edu.sg
Y. Wang, G. Adamo, J. Tian[+], C. Soci
Division of Physics and Applied Physics
School of Physical and Mathematical Sciences
Nanyang Technological University
21 Nanyang Link, Singapore 637371, Singapore
Y. Wang
Interdisciplinary Graduate School
Energy Research Institute @NTU (ERI@N)
Nanyang Technological University
50 Nanyang Drive, Singapore 637553, Singapore
S. T. Ha
Institute of Materials Research and Engineering
Agency for Science Technology and Research (A*STAR)
2 Fusionopolis Way, Singapore 138634, Singapore

The ORCID identification number(s) for the author(s) of this article can be found under https://doi.org/10.1002/adma.202412952

[+]Present address: School of Engineering, Westlake University, Hangzhou, Zhejiang 310024, China

DOI: 10.1002/adma.202412952

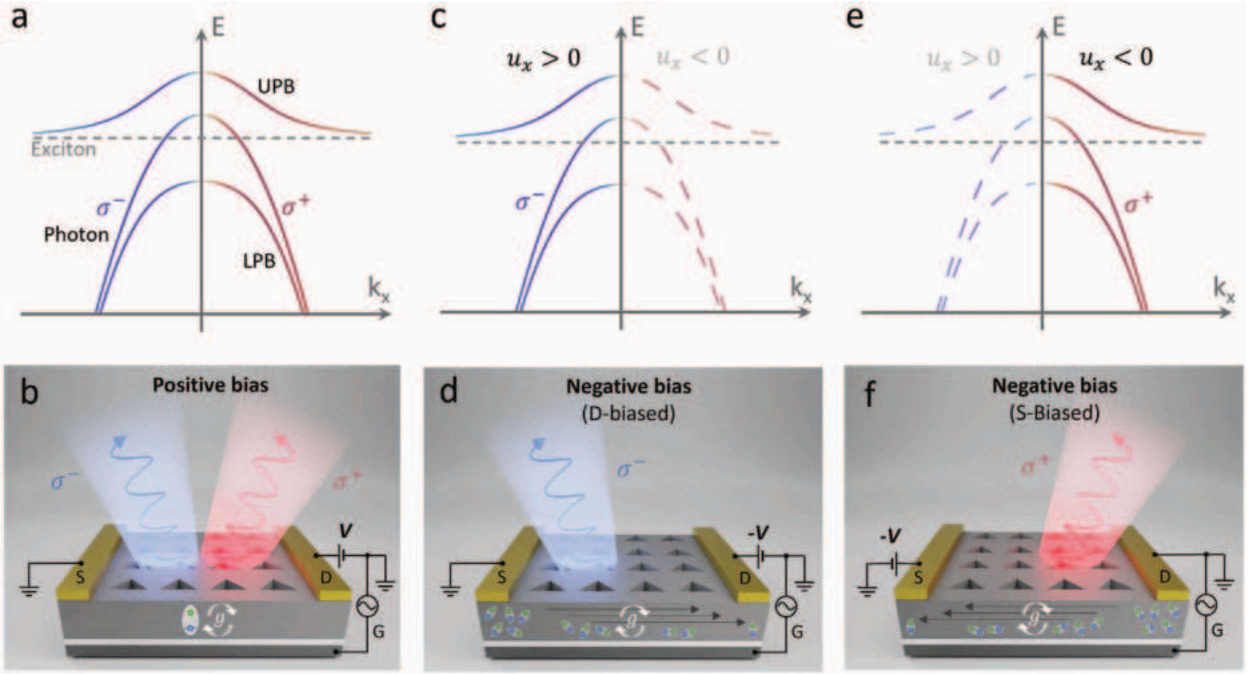

Figure 1. Tunable spin-polarized exciton-polaritons in the electrically driven perovskite metatransistor. The light-emitting metatransistor operates in two distinct modalities: i) generates circularly polarized EL from exciton polaritons of opposite spin, as prescribed by the polaritonic Rashba effect and ii) unidirectionally emits circularly polarized light from spin-down and spin-up exciton polaritons with either positive or negative group velocities. a) Characteristic band diagram of a metasurface with broken in-plane inversion symmetry, for the case of passive photonic modes and exciton-polariton bands, where the spin degeneracy is lifted due to the optical and polaritonic Rashba effect, respectively. The red and blue colours denote spin-up and spin-down states, respectively. b) Schematic of Rashba polariton emission from the electrically driven metasurface under positive drain bias, operating in modality i). c,e) Dispersion of the optical bands with lifted spin degeneracy featuring positive ($u_x > 0$) and negative group velocities ($u_x < 0$), both for photon and polariton modes; bands with unmatched group velocities are not populated (dashed lines). d,f) Schematics of spin polarized emission from the device operating in modality ii), with negative drain bias (D-biased condition) or negative source bias (S-biased condition). Spin-momentum locking and asymmetric exciton generation enable electrical control of directionality and helicity of the spin polarized polaritonic emissions.

(a phenomenon also referred to as the optical Rashba effect,[35–38] in analogy with the condensed matter Rashba effect[39–41]). Usually, this comes at the expense of lowering the Q-factor of the modes, weakening the coupling strength at C-points.

Here we demonstrate the electrical generation and control of highly spin-polarized exciton polaritons in a perovskite light-emitting metatransistor. The device combines, in a monolithic structure, a dielectric metasurface designed to break the in-plane inversion symmetry and a dielectric stack that breaks the out-of-plane inversion symmetry, resulting in purely circularly polarized resonances with high Q-factors. By supporting strong coupling of the highly confined excitons in the perovskite, this system yields exciton polaritons with spin purity approaching the theoretical limit. Upon charge injection in the transistor channel, we observe electroluminescence (EL) characterized by a marked *polaritonic* Rashba effect (the spin-split of polariton bands in opposite halves of the momentum space[42]). Moreover, we show that individual polaritonic spin states can be selected electrically by controlling charge (exciton) injection and thus imparting specific directionality and helicity to the circularly polarized EL.

2. Device Concept

The electrically driven light emitting metasurface adopts a typical top-contact, bottom-gate light emitting transistor (LET) configuration, so that the excitonic emission channel and the metasurface pattern can be colocated between the source and drain electrodes.[43] The metasurface is directly fabricated into the $MAPbI_3$ film with high uniformity, by focused ion beam (FIB) lithography. The LET configuration enables operation of the device in the ambipolar transport regime under certain electrical biasing conditions, where electrons and holes are simultaneously injected from the source and the drain electrodes into the transistor channel at the semiconductor-insulator interface, and form excitons that radiatively recombine to emit light.[44,45] Moreover, tuning of the relative bias between source and drain electrodes enables control of the lateral position of the recombination zone within the transistor channel,[46] a unique feature which here we exploit to implement electrical control of the directional energy flow of exciton-polaritons and their spin in symmetry-broken BIC metasurfaces operating in the strong coupling regime (**Figure 1**).

In practice, our light-emitting *metadevices* can operate in two modes: i) generate EL emission from exciton polaritons of opposite spin, as prescribed by the polaritonic Rashba effect (Figure 1a,b) and ii) emit unidirectional light stemming from exciton polaritons with spin-down (Figure 1c,d) or spin-up (Figure 1e,f) into the left or the right halves of the outcoupling hemisphere. Figure 1a illustrates the optical dispersion of the passive photonic mode in the broken symmetry metasurface that lifts the spin degeneracy. The photonic mode encompasses spin-up states for $k_x > 0$ and spin-down states for $k_x < 0$ in the opposite halves of the momentum space (colored in red and blue, respectively). Upon strong coupling, the anticrossing of the photonic mode and the perovskite exciton leads to the emergence of upper polariton bands (UPB) and lower polariton bands (LPB), inheriting the spin properties of the photonic band. When the transistor is operated under positive drain bias ($V_d > 0$), excitons are generated uniformly within the metasurface and exciton polaritons with *opposite spins that decay radiatively outcouple from the metasurface in opposite directions (Figure 1b)*. When photons and polaritons of positive (negative) group velocity $u_x = (1/\hbar)\mathrm{d}E/\mathrm{d}k_x$ propagate in the metasurface, the spin-down (spin-up) branch is selectively populated, as shown in Figure 1c (Figure 1e). Combined with spin-momentum locking, the change of group velocity within the metasurface induced by negative bias applied to either the drain ($V_d < 0$) or source ($V_s < 0$) electrodes enables electrical control of helicity and directionality of the light emitted by spin-polarized polaritons (Figure 1d,f).

3. Strong Coupling in High-Q Perovskite Metasurface with Broken Inversion Symmetry

Methylammonium lead iodide ($MAPbI_3$) perovskite was selected for this proof-of-principle demonstration of an electrically driven spin-polarized polariton light-emitting device because it combines excellent excitonic and charge transport properties.[47–50] Its high refractive index also allows for monolithic fabrication of metasurfaces[51–53] in light-emitting transistor devices. Absorption measurements of a pristine $MAPbI_3$ film at 78 K yield exciton energy of $E_{\text{exc}} = 1.693$ eV and damping rate of $\gamma_{\text{exc}} = 68$ meV using the Elliot model fitting (Note S1 and Figure S1, Supporting Information). The exciton binding energy extracted from the model ($E_b \approx 30$ meV) is larger than the thermal energy even at room temperature, fulfilling the prerequisite for the formation of stable exciton-polaritons.[47] The low temperature electrical characteristics of the $MAPbI_3$ perovskite reveal slightly unbalanced ambipolar charge carrier injection, with higher mobility observed for electrons (Note S2 and Figure S2, Supporting Information).

Our monolithic metasurface design uses an isosceles triangular hole unit cell, with broken in-plane inversion symmetry (**Figure 2**a,b).[36,37,54] The optical response of the perovskite metasurface was numerically evaluated by modelling the refractive index of $MAPbI_3$ as a Tauc-Lorentz dielectric, both in the absence and presence of excitons (Note S3 and Figure S3, Supporting Information). The band structure of the passive perovskite metasurface in the absence of excitons, calculated by eigenmode simulations, displays a pair of pure σ^+ and σ^- states ($|S_3| = 1$) adjacent to the Γ-point on the Ph_2 band, as seen in Figure 2c. These circularly polarized states, known as C-points, emerge from the splitting of the polarization singularity (V-point) of the symmetry-protected BIC upon breaking the in-plane inversion symmetry of the metasurface. The electric field distribution of the Ph_2 band shows a quadrupole mode strongly confined within the perovskite material (Figure S4, Supporting Information), favoring the strong interaction of perovskite excitons and cavity photons. Conventionally, in a triangular hole metasurface, where only the in-plane IS is broken, the Q-factor for the Ph_2 band peaks at the Γ-point. Here the mode is linearly polarized in the far field ($|S_3| = 0$) and the Q-factor strongly decreases toward the C-points, as shown in the upper panel of Figure 2d. Recently, it was shown that high Q-factor points can be created anywhere off Γ exploiting the hybridization of photonic resonances when the out-of-plane symmetry of the system is broken;[55] alternatively, one of the C-points could be shifted to the high-Q Γ-point through a slant along the vertical axis of the metasurface unit cell.[56,57] Here we make use of the transistor stack, which breaks the out-of-plane symmetry by design (Figure 2a), and optimize the thickness of the SiO_2 dielectric layer (500 nm) between the Si substrate and the perovskite film to produce two high Q-factor modes at the C-points (at $k_x = \pm 0.125\ \mu\text{m}{-}^{1}$) on the Ph_2 band (lower panel of Figure 2d). The creation of these high-Q points stems from the interplay between Ph_1 and Ph_2 bands, which would be nearly degenerate in the absence of vertical symmetry breaking. A detailed investigation of the symmetry-dependent Q factor for the modes in the Ph_2 band can be found in Note S4 and Figure S5, Supporting Information). It is worth noting that our design strategy allows enhancing the Q-factor of both circularly polarized photonic modes without requiring additional layers or complex fabrication steps, offering a simple route to achieve spin-polarized polaritonic emission from electrically driven devices.

Excitonic states with energy E_{exc} within the monolithic metasurface coherently couple to spin-momentum locked photonic modes with good spectral overlap (Figure 1b). The energy of the resulting upper and lower polariton states can be calculated according to the coupled oscillator model[3]

$$E_{\text{UP,LP}} = \frac{1}{2}\left(E_{\text{cav}} + i\gamma_{\text{cav}} + E_{\text{exc}} + i\gamma_{\text{exc}}\right) \pm \frac{1}{2}\sqrt{4g^2 + \left[E_{\text{exc}} + i\gamma_{\text{exc}} - E_{\text{cav}} - i\gamma_{\text{cav}}\right]^2} \tag{1}$$

where E_{cav} and γ_{cav} are the energy and the damping rate of the metasurface photonic modes, while E_{exc} and γ_{exc} the energy and the damping rate of the excitonic mode of the perovskite. g is the coupling strength between the two modes. The corresponding Rabi splitting energy is $\Omega_R = 2\sqrt{g^2 - \frac{(\gamma_{\text{cav}} - \gamma_{\text{exc}})^2}{4}}$, which corresponds to the smallest energy difference between the upper and lower polariton bands. The simulated angle-resolved reflection spectra of the active perovskite metasurface (in the presence of excitons), plotted in Figure 2e, show excellent agreement with the experimental angle-resolved reflection spectra of Figure 2f. The white and green solid lines in Figure 2f illustrate the dispersion of the photonic modes Ph_2 and Ph_5 in the passive metasurface (see Figure 2c), whereas the white and green dashed lines show the dispersion of the polaritonic bands formed by the $MAPbI_3$ exciton coupled to the photonic modes Ph_2 (LPB_2, UPB_2) and Ph_5 (LPB_5, UPB_5), respectively. The best fit to Equation (1) yields Rabi splitting energies of the polaritonic bands associated to Ph_2 and Ph_5 of $g_{\text{Ph2}} = 116$ meV and $g_{\text{Ph5}} = 138$ meV. The difference between the two could be attributed to the different mode profile and dispersion of the Ph_2 and Ph_5 photonic modes.[58] The Rabi splitting energy of polaritonic bands fulfil the criteria $\Omega_R > \gamma_{\text{exc}} + \gamma_{\text{cav}}$, i.e., $g > \sqrt{({\gamma_{\text{exc}}}^2 + {\gamma_{\text{cav}}}^2)/2}$. For our two sets of polaritonic bands, the linewidths of the photonic modes obtained from the simulated spectra are $\gamma_{\text{cav}_{\text{Ph2}}} = 0.5$ meV and $\gamma_{\text{cav}_{\text{Ph5}}} = 0.6$ meV, thus confirming that the system is in a strong coupling regime. The absence of the higher energy upper polariton bands (above

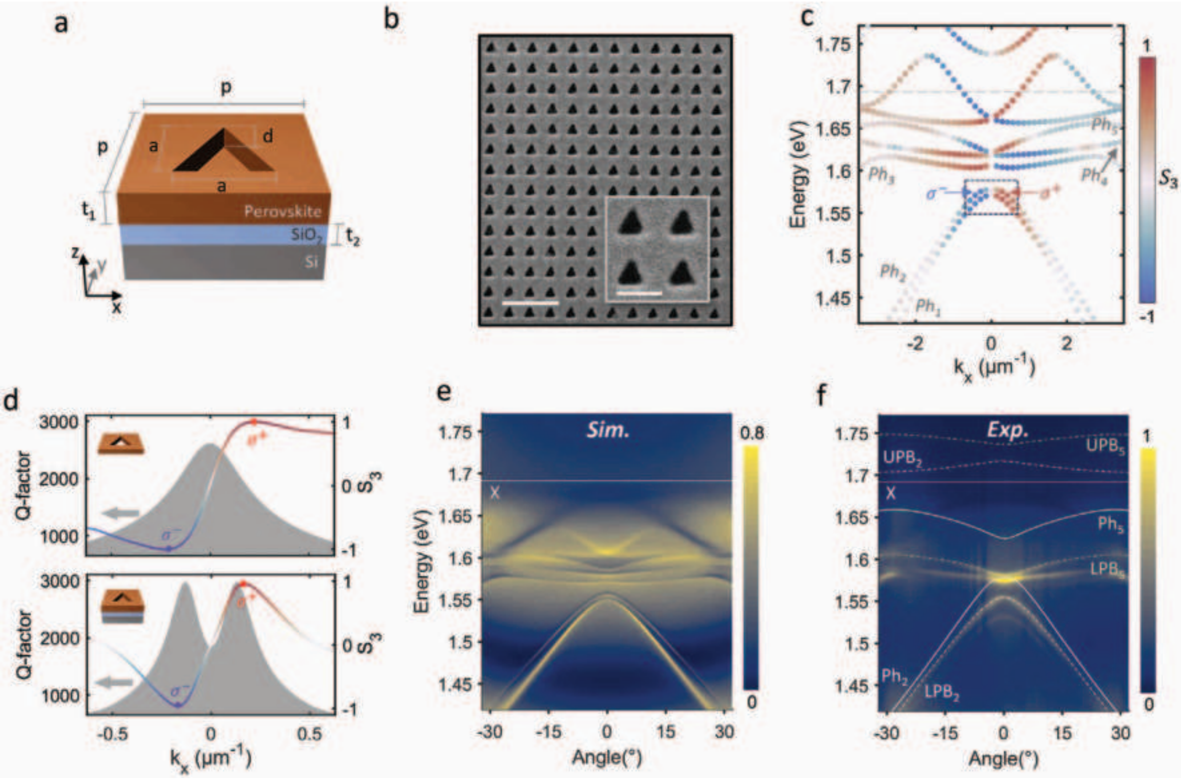

Figure 2. Engineering strong chiral light–matter interaction in perovskite metasurfaces with broken inversion symmetry. a) Schematic of the quasi-BIC unit cell on a SiO_2-Si substrate. The geometric parameters are set as follows: period $p = 355$ nm, base and height of the triangular hole $a = 0.6 \times p$, thickness of the perovskite film $t_1 = 350$ nm, depth of the triangle hole $d = 250$ nm, thickness of the SiO_2 layer $t_2 = 500$ nm. b) Scanning electron microscope image of the fabricated perovskite metasurface. The scale bar is 1 µm. The inset shows an enlarged view of four unit cells. The scale bar is 300 nm. c) Numerically simulated passive photonic bands of the perovskite metasurface with broken in-plane and out-of-plane inversion symmetry (IS). The colormap indicates the value of the normalized Stokes parameter S_3. The gray dashed line denotes the energy of the excitonic mode of the $MAPbI_3$ perovskite. d) Simulated Q-factor (shaded areas) and S_3 (colored lines) of the photonic Ph_2 band for a passive perovskite metasurface with only the in-plane IS breaking (upper panel) and both in-plane and out-of-plane IS breaking (lower panel), showing the emergence of two high-Q peaks in correspondence of the C-points (blue and red dots). The insets show the schematic of the two designs. e) Simulated angle-resolved reflection spectra of the active perovskite metasurface, when accounting for the $MAPbI_3$ exciton. The white solid line denotes the excitonic mode of perovskite (X). f) Experimental angle-resolved reflection spectra of the perovskite metasurface. The white and green solid lines illustrate the dispersion of two passive photonic modes (Ph_2 and Ph_5 bands). The white and green dashed lines denote the dispersion of the corresponding polariton bands for Ph_2 (LPB_2, UPB_2) and Ph_5 (LPB_5, UPB_5), respectively.

1.693 eV) in both the simulated and experimental spectra is due to the strong absorption of the perovskite above the band edge. The angle-resolved photoluminescence measurement upon nonresonant optical pumping, presented in Figure S8 in the Supporting Information, demonstrates the substantial occupation of spin-polarized polaritons in the LPBs, as predicted by the coupled oscillator model. The Hopfield coefficients of the LPB_2 band indicate a high exciton fraction of ≈0.2 (Figure S9, Supporting Information), showing good potential for polariton condensation into the spin states.

4. Electrically Driven Polaritonic Rashba Effect

We exploit the light-emitting transistor functionality to control charge injection into the perovskite metasurface and induce strong coupling of the excitons with designer photonic modes. To improve brightness and uniformity of the electroluminescence emitted from the transistor channel, the gate bias is AC-modulated while the balance of electron and hole injection is controlled by DC source-drain bias.[59] Under positive bias conditions ($V_s = 0$ V, $V_d = 90$ V and $|V_g| = 90$ V), we observe a uniform distribution of radiative excitons across the metasurface, as seen in Figure S8a in the Supporting Information. The measured angle-resolved EL spectra shown in **Figure 3a** reveal intense emission from the LPBs, in good agreement with calculations (dashed line). The monolithic device architecture enables efficient light–matter interaction, so that the signal from the uncoupled excitons is barely visible in the spectra. As spin-polarized polaritons decay as circularly polarized photons and outcouple from the metasurface inheriting the same energy and momentum, the spin-dependent polaritonic band structure can be determined from circularly polarized EL measurements. The spin properties of the polaritons are characterized by the normalized Stokes parameter, $S_3 = \frac{I_{\sigma^+} - I_{\sigma^-}}{|I_{\sigma^+} + I_{\sigma^-}|}$, which can be mapped in the k-space. Angle-resolved EL spectra of opposite polarization handedness σ^+ (Figure 3b) and σ^- (Figure 3c) reveal the polaritonic Rashba effect, i.e., the splitting of the electrically driven

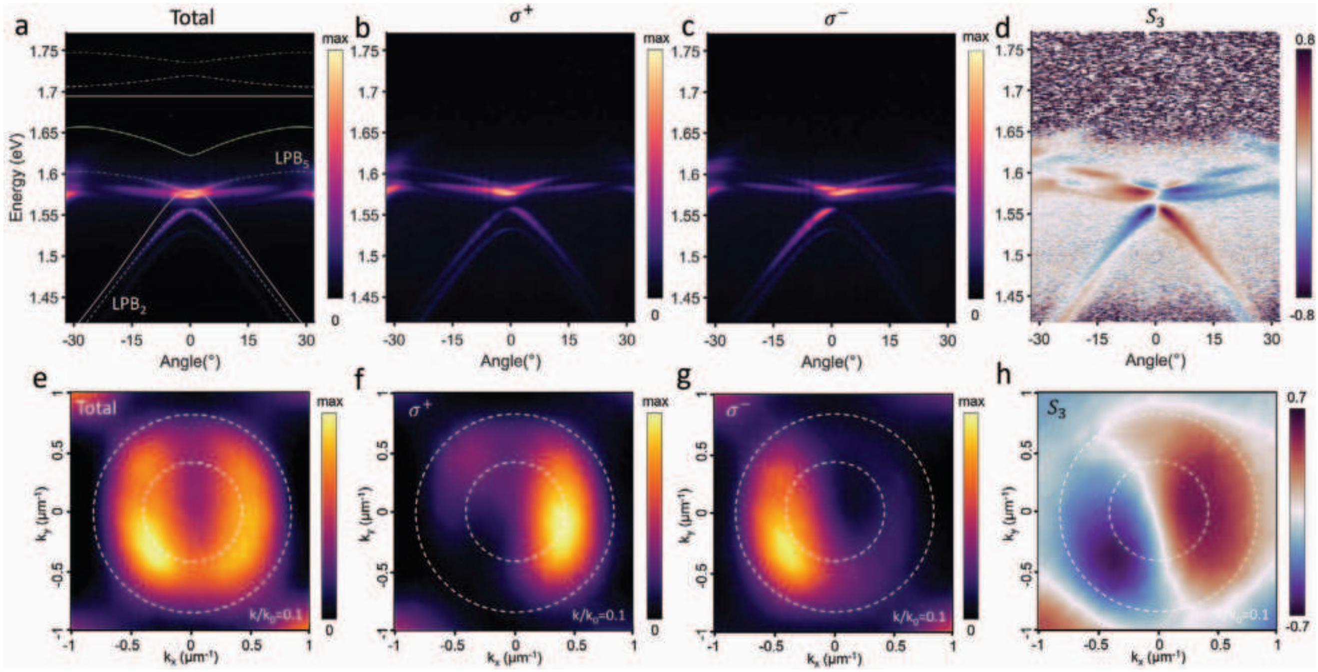

Figure 3. Electrically driven polaritonic Rashba effect from light-emitting perovskite metasurfaces. a) Total angle-resolved electroluminescence (EL) spectra for the perovskite metasurface under the positive bias condition with $V_s = 0$ V, $V_d = 90$ V, and $|V_g| = 90$ V, showing symmetrically distributed polaritonic states around the normal direction ($k_x = 0$). The solid lines denote the dispersion of the excitonic and photonic modes while the dashed lines represent polaritonic bands, as defined in Figure 2f. b,c) The right-circularly (σ^+) and left-circularly (σ^-) polarized angle-resolved EL spectra show mirror symmetric distributions with respect $k_x = 0$. d) The S_3 colormap of the EL dispersion reveals highly pure, spin-polarized bands, a clear manifestation of the polaritonic Rashba effect. e–g) 2D momentum space images of the total, right-circularly polarized (σ^+) and left-circularly polarized (σ^-) polaritonic EL, obtained at the energy of 1.55 eV with a 10 nm band-pass filter. h) The corresponding S_3 colormap in the 2D k-space.

spin-polarized exciton polaritons, with σ^+ and σ^- LPBs appearing as mirror images in k-space. The corresponding S_3 map, shown in Figure 3d, indicates a very high degree of circular polarization, reaching a maximum of ≈0.8 in the LPB$_2$ near ± 2°, a value remarkably close to the calculated $|S_3| = 1$, when accounting for imperfections induced by the metasurface fabrication. As discussed in Figure 2d, we observe enhanced Q-factors that peak near the C-points in the EL spectra, revealed by the reduced linewidth (Figure S7, Supporting Information) and the ≈11-fold maximum enhancement of the EL from the LPB$_2$ at the same angle. Figure 3e–g illustrates the total, right circularly polarized, and left circularly polarized far-field profiles of the polaritonic emission from LPB$_2$ in the vicinity of the Γ-point, collected using a 10 nm bandwidth (≈20 meV) bandpass filter centered around 1.55 eV. The corresponding S_3, shown in Figure 3h, reveals the high purity of the spin-polarized polaritons, with an integrates $|S_3|$ value reaching ≈0.7, consistent with the anisotropy map in Figure 3d. Additional field patterns of the Rashba polaritons obtained at different EL energies are illustrated in Figure S10 in the Supporting Information.

5. Electrical Control of Spin-Polarized Exciton Polaritons

The unique device functionality of the light-emitting metatransistor allows to select momentum and spin of exciton polaritons by simply adjusting the source–drain biasing conditions. While under positive bias condition ($V_d > 0$, Figure 1b) the distribution of excitons within the channel is uniform, under the S-biased condition ($V_s = -90$ V, $V_d = 0$ V, and $|V_g| = 80$ V, Figure 1d) excitons are predominantly formed and concentrated near the drain electrode; conversely, under the D-biased condition ($V_s = 0$ V, $V_d = -90$ V, Figure 1f), excitons concentrate near the source electrode. This is clearly seen in the optical images of the emitting device in real space, where distinct EL gradients across the channel can be observed in S- and D-biased conditions (insets of **Figures** 4a,b and S11, Supporting Information). The corresponding charge injection mechanisms are discussed in Note S5 in the Supporting Information and illustrated in Figure S12 in the Supporting Information.

Asymmetric exciton distributions in the transistor channel result in the excitation of photonic modes with specific in-plane group velocity, similarly to what had been shown in simulations reported in ref. [34] (Figure S7, Supporting Information). Experimentally, polariton modes with defined group velocity were demonstrated upon injection of propagating polaritons through the boundaries of a BIC metasurface.[10] In our device, polaritons are generated preferentially on the drain or source side of the metasurface upon electrical charge injection. When excitons accumulate on the left side of the metasurface, only photonic modes with $u_x > 0$ are populated, forming polaritons that propagate in the + x direction and decay as photons carrying the corresponding energy and momentum. Likewise, when excitons are formed at the right side of the metasurface, the emission derives primarily from polaritons with negative in-plane group velocity $u_x < 0$. It has to be noted that the polariton group velocity is linked

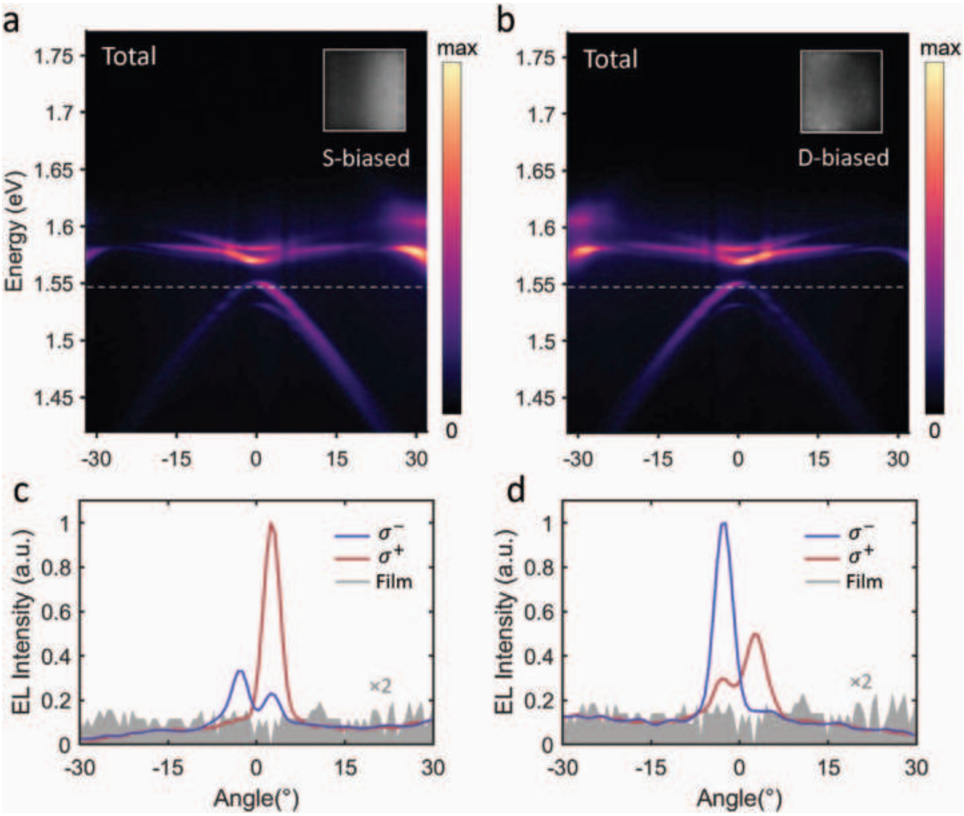

Figure 4. Electrically tunable polariton spins and directionality from light-emitting perovskite metasurfaces. a,b) The total angle-resolved electroluminescence spectra, under D-biased and S-biased conditions, show a remarkable resemblance to the right- and left-circularly polarized EL spectra of Figure 3b,c, thus demonstrating selective population of the spin-polariton modes. The insets show the real images of the EL emission from the perovskite metasurface, under the respective bias condition. c,d) Spin-polarized polaritonic EL intensity at 1.545 eV (white dashed lines in Figure 4a,b), exhibiting a strong degree of circular polarization at ±2°. The gray shaded areas indicate the angle dependent EL intensity of the unpatterned perovskite film, at the same photon energy.

to its spin state. Since the metasurface has broken IS but maintains translational symmetry, both the chirality and the group velocity of the polaritonic bands are antisymmetric with respect to the k_y-k_z plane ($k_x = 0$), i.e., $S_3\,(-k_x) = -S_3(k_x)$ and $u\,(-k_x) = -u(k_x)$. Thus, as the group velocities associated with each pair of circularly polarized states spawning from the BIC are characterized by opposite signs ($u_{\sigma^+} = -u_{\sigma^-}$), the spin states of the polaritons can be selected by controlling the sign of the group velocity.

Figure 4a,b shows the angle-resolved EL spectra of the device under S-biased and D-biased conditions, demonstrating efficient population of either the right or the left halves of the LPB_2 band. To depict the spin state of the excited polaritons on the LPB_2 band, the angle-dependent circularly polarized EL intensity at the energy of 1.545 eV, under the two biasing conditions, are shown in Figure 4c,d. Unlike the positive bias case, characterized by equally populated spin-polarized polariton bands (Figure 3), in the S-biased device we detect strong chiral EL with $S_3 = 0.67$ primarily from the σ^+ polaritons at +2°, while the EL of the σ^- state is significantly suppressed (Figure 4c). On the other hand, enhanced chiral EL with $S_3 = -0.54$ from the σ^-polaritons at −2° is observed in the D-biased device (Figure 4d). This demonstrates electrical selection of spin states and directionality of the exciton polaritons.

The strong enhancement of the spin-polarized polaritonic emission at ±2°, compared to the excitonic emission of the bare perovskite film (shaded areas in Figure 4c,d), is due to the high Q-factor near the C-points, discussed in Figure 2d. It shall be noted that it is possible to tune the chiral EL emission angle by adjusting the polariton energy away from the C-points, albeit at the cost of sacrificing spin purity (a reduction of S_3), as shown in Figure S13 in the Supporting Information.

In addition to the electrical selection of polariton spin states that emit in opposite directions from a single metasurface, the design of pixelated metasurfaces can be employed to implement electrical switching between polaritons with opposite spins emitting in a given direction. For instance, this is possible using two metasurfaces with 180°-rotated triangular holes positioned next to the source and drain electrodes (Figure S14, Supporting Information). Under S-biased or D-biased conditions, the emission from each pixel can be assumed to be uniform. When transitioning between the two pixels by switching from the S-biased to the D-biased condition, the EL emission intensity in a given direction remains nearly unchanged, but its polarization is flipped (Figure S14, Supporting Information). This provides an alternative route for spin polariton control when fixed emission directionality is required, such as to realize polarized light sources for quantum information processing.

6. Conclusion

In conclusion, our study has successfully demonstrated the generation of directional spin-polarized exciton polaritons from monolithic dielectric metasurfaces upon electrical injection, a feat previously accomplished only in optically pumped microcavities. The monolithic integration offers significant advantages by enhancing light–matter interaction and reducing the overall complexity of the system. In our work, the broken in-plane IS of the metasurface lifts the spin degeneracy of the photonic modes, while the broken out-of-plane IS enhances the Q-factor of the spin states. Strong coupling is achieved between the electrically injected perovskite excitons and the cavity photons at 78 K, with the Rabi splitting energy of ≈120 meV and high purity of directional spin-polarized polaritons ($|S_3| = 0.8$).

Leveraging on spin-momentum locking, the unique functionality of the light-emitting transistor allows asymmetric exciton injection under different biasing conditions, providing the capability to electrically control the spin state and directionality of the polaritonic emission. This platform could be readily extended to implement electrical tunability of other characteristics of exciton polariton emission, e.g., amplitude and phase, simply by varying the metasurface design. Thus, we believe this accomplishment takes a significant step toward the integration of polariton spintronic technologies with electronics, facilitating the practical realization of polaritonic devices and architectures such as electrically driven and tunable inversionless spin lasers, or spin logic circuits.

7. Experimental Section

Numerical Simulations: The eigenmode simulations for the photonic band structure, Q-factor, and normalized Stokes parameter were conducted employing COMSOL Multiphysics 5.4. Floquet periodic boundary conditions were applied in the transverse direction, while perfectly matched layers were utilized in the *z*-direction. The Stokes parameter was determined by simulating the far-field Jones vector $[\widetilde{E_x}, \widetilde{E_y}]^T$ of the eigenmode. Angle-resolved reflection spectra were simulated using rigorous coupled wave analysis within the Ansys Lumerical software. The refractive index of the $MAPbI_3$ perovskite at 78 K was derived from tabulated permittivity data in ref. [48], fitting the data with a Tauc-Lorentz model. This methodology facilitated the extraction of optical constants with and without excitonic resonance. Further details are provided in Note S1 in the Supporting Information.

Material Synthesis: $MAPbI_3$ thin films were synthesized using a solution-processed spin-coating method. Methylammonium iodide (CH_3NH_3I, MAI) was procured from Greatcell, lead iodide (PbI_2, 99.99%) from Tokyo Chemical Industry Co. Ltd., and anhydrous dimethylformamide (DMF) from Sigma-Aldrich. All chemicals were used as received without purification. The 1.2 м MAPbI3 precursor solution was prepared by dissolving MAI and PbI_2 powder in DMF with a molar ratio of 1:1. After magnetic stirring for 2 h at 273 K in a N_2-filled glovebox, the solution was filtered through a polyvinylidene fluoride syringe filter (0.45 µm) before spin-coating. Substrates, heavily p-doped Si with a thermally grown SiO_2 (500 nm) layer, were cleaned with ultrasonication in acetone, isopropanol, and deionized water. Following drying and an oxygen plasma cleaning treatment, the perovskite precursor solution was spin-coated onto the substrates with a speed of 4900 rpm for 35 s using the antisolvent deposition method, with toluene drop-cast on the substrates 5 s after starting spinning. The resulting films were finally annealed at 373 K for 15 min, yielding a 350 nm thickness film, as indicated by atomic force microscopy in Figure S15 in the Supporting Information.

Light Emitting Device and Metasurface Fabrication: The perovskite light emitting device adopts the similar lateral configuration of a thin film field effect transistor using a bottom-gate and top-contact configuration. After the perovskite thin film fabrication, 100 nm thick Au electrodes were thermally evaporated in high vacuum (≈10–^{6} mbar) using a shadow mask. To avoid thermal decomposition of the perovskite films, samples were placed on a water-cooled substrate holder at 291 K during the electrode deposition. The resulting LET channel length (L) and width (W) were 80 µm and 1 mm, respectively. The perovskite metasurface fabrication was conducted by FIB lithography process. A 40 µm × 40 µm triangular air hole array was patterned between the source and drain electrodes using the Helios 600 NanoLab, FEI system. The ion beam current was controlled around ≈4 pA for suitable spot size of etching.

Electrical and Optical Characterization: Electrical and optical characterization was carried out using a temperature-controlled probe stage (HFS600E-PB4/PB2, Linkam) at the temperature of 78 K in the dark and under vacuum (≈10–^{3} mbar). DC measurements for the transfer characteristics were acquired with a two-channel precision source/measure unit (B2902A, Agilent). Charge-carrier mobilities were extracted from the forward sweeping of transfer characteristics obtained at $V_{ds} = 80$ V, using the conventional equations for metal-oxide semiconductor transistors in the saturation regime: $\mu_{sat} = \frac{2L}{WC_i} \left(\frac{\partial\sqrt{I_{ds}}}{\partial V_g}\right)^2$.

The photoluminescence (PL) and EL measurements were performed with a home-built microspectrometer. The system consists of an inverted optical microscope (Nikon Ti-U), a spectrograph (Andor SR-303i with 150 lines mm^{-1} grating), and an electron-multiplying charged-coupled detector (Andor Newton 971). The PL spectra of the perovskite film were taken when the sample was excited by a 405 nm continuous wave solid state laser with a spot size of ≈15 µm in diameter. The EL measurements of unpatterned light emitting devices were performed on the same optical setup under positive bias mode of $V_s = 0$ V, $V_d = 90$ V and AC gate voltage of $|V_g| = 80$ V (100 kHz modulation frequency), using an arbitrary waveform generator (3390, Keithley) coupled with a high-voltage amplifier (WMA-300, Falco Systems). The optical images of the operating device were taken and acquired by a cooled scientific Complementary Metal–Oxide–Semiconductor (sCMOS) scientific camera (PCO.edge 3.1 m) coupled to the optical microscope.

Angle-Resolved Measurements: The angle resolved reflection, PL, and EL measurements of the perovskite metasurface were also performed in the home-built microspectrometer setup. A lens system along the light path between the microscope and the spectrograph is used to project the back focal plane of the collection objective (Nikon ×50, with numerical aperture, NA = 0.45) onto the slit of the spectrograph. This configuration allows spectral or spatial measurement with angular information corresponding to the NA of the objective. A pinhole in the detection path is used as a spatial filter to collect the signal only from the center of the metasurface, which mitigates the edge effects. A linear polarizer and quarter waveplate placed on the optical path of the lens system were used to select the collection polarization. A halogen white light was used as the light source for the reflection measurement. The angle-resolved PL and EL spectra were taken using the same pumping scheme as the previous section. The EL spectra with S-biased and D-biased conditions were conducted in the same setup by changing the electrical bias on the source and drain electrodes.

Supporting Information

Supporting Information is available from the Wiley Online Library or from the author.

Acknowledgements

Research was supported by the Singapore Ministry of Education (Grant no. MOE-T2EP50222-0015) and by the Agency for Science, Technology and Research, A*STAR (A*STAR-AME Grant no. A18A7b0058). S.T.H. acknowledges support from A*STAR MTC-Programmatic (Grant no. M21J9b0085).

Conflict of Interest

The authors declare no conflict of interest.

Author Contributions

C.S., J.T., G.A., and Y.W. conceived the idea and planned the research. Y.W. fabricated the perovskite devices, performed the electrical and optical characterization of the sample, and conducted the theoretical analysis, numerical simulations, and data processing. G.A. fabricated the metasurfaces. S.T.H. and J.T. contributed to optical characterization and J.T. helped with numerical simulations. Y.W, J.T., G.A., and C.S. performed data analysis and wrote the paper with inputs from S.T.H. C.S. and G.A. supervised the work.

Data Availability Statement

The data that support the findings of this study are openly available in Nanyang Technological Univeirsity (NTU) Research Data Repository DR-NTU at https://doi.org/10.21979/N9/EGB3GG, reference number 60.

Keywords

electrical injection polaritons, electrically-tunable metadevices, light emitting transistors, Perovskite metasurfaces, Spin-polarized exciton-polaritons

Received: August 30, 2024
Revised: October 18, 2024
Published online: November 26, 2024

---

[1] J. Kasprzak, M. Richard, S. Kundermann, A. Baas, P. Jeambrun, J. M. Keeling, F. M. Marchetti, M. H. Szymanska, R. Andre, J. L. Staehli, V. Savona, P. B. Littlewood, B. Deveaud, S. le Dang, *Nature* **2006**, *443*, 409.
[2] A. Amo, J. Lefrère, S. Pigeon, C. Adrados, C. Ciuti, I. Carusotto, R. Houdré, E. Giacobino, A. Bramati, *Nat. Phys.* **2009**, *5*, 805.
[3] H. Deng, H. Haug, Y. Yamamoto, *Rev. Mod. Phys.* **2010**, *82*, 1489.
[4] T. Byrnes, N. Y. Kim, Y. Yamamoto, *Nat. Phys.* **2014**, *10*, 803.
[5] G. Lerario, A. Fieramosca, F. Barachati, D. Ballarini, K. S. Daskalakis, L. Dominici, M. De Giorgi, S. A. Maier, G. Gigli, S. Kéna-Cohen, D. Sanvitto, *Nat. Phys.* **2017**, *13*, 837.
[6] D. Ballarini, M. De Giorgi, E. Cancellieri, R. Houdre, E. Giacobino, R. Cingolani, A. Bramati, G. Gigli, D. Sanvitto, *Nat. Commun.* **2013**, *4*, 1778.
[7] R. Tao, K. Peng, L. Haeberle, Q. Li, D. Jin, G. R. Fleming, S. Kena-Cohen, X. Zhang, W. Bao, *Nat. Mater.* **2022**, *21*, 761.
[8] D. Ballarini, A. Gianfrate, R. Panico, A. Opala, S. Ghosh, L. Dominici, V. Ardizzone, M. De Giorgi, G. Lerario, G. Gigli, T. C. H. Liew, M. Matuszewski, D. Sanvitto, *Nano Lett.* **2020**, *20*, 3506.
[9] D. Sanvitto, S. Kena-Cohen, *Nat. Mater.* **2016**, *15*, 1061.
[10] V. Ardizzone, F. Riminucci, S. Zanotti, A. Gianfrate, M. Efthymiou-Tsironi, D. G. Suarez-Forero, F. Todisco, M. De Giorgi, D. Trypogeorgos, G. Gigli, K. Baldwin, L. Pfeiffer, D. Ballarini, H. S. Nguyen, D. Gerace, D. Sanvitto, *Nature* **2022**, *605*, 447.
[11] K. Peng, R. Tao, L. Haeberle, Q. Li, D. Jin, G. R. Fleming, S. Kena-Cohen, X. Zhang, W. Bao, *Nat. Commun.* **2022**, *13*, 7388.
[12] A. Graf, M. Held, Y. Zakharko, L. Tropf, M. C. Gather, J. Zaumseil, *Nat. Mater.* **2017**, *16*, 911.
[13] C. Schneider, A. Rahimi-Iman, N. Y. Kim, J. Fischer, I. G. Savenko, M. Amthor, M. Lermer, A. Wolf, L. Worschech, V. D. Kulakovskii, I. A. Shelykh, M. Kamp, S. Reitzenstein, A. Forchel, Y. Yamamoto, S. Hofling, *Nature* **2013**, *497*, 348.
[14] P. Bhattacharya, T. Frost, S. Deshpande, M. Z. Baten, A. Hazari, A. Das, *Phys. Rev. Lett.* **2014**, *112*, 236802.
[15] A. Kavokin, T. C. H. Liew, C. Schneider, P. G. Lagoudakis, S. Klembt, S. Hoefling, *Nat. Rev. Phys.* **2022**, *4*, 435.
[16] A. Amo, T. C. H. Liew, C. Adrados, R. Houdré, E. Giacobino, A. V. Kavokin, A. Bramati, *Nat. Photonics* **2010**, *4*, 361.
[17] J. Liang, W. Wen, F. Jin, Y. G. Rubo, T. C. H. Liew, R. Su, *Nat. Photonics* **2024**, *18*, 357.
[18] K. Łempicka-Mirek, M. Król, H. Sigurdsson, A. Wincukiewicz, P. Morawiak, R. Mazur, M. Muszyński, W. Piecek, P. Kula, T. Stefaniuk, M. Kamińska, L. De Marco, P. G. Lagoudakis, D. Ballarini, D. Sanvitto, J. Szczytko, B. Piętka, *Sci. Adv.* **2022**, *8*, eabq7533.
[19] Y. Li, X. Ma, X. Zhai, M. Gao, H. Dai, S. Schumacher, T. Gao, *Nat. Commun.* **2022**, *13*, 3785.
[20] T. P. Lyons, D. J. Gillard, C. Leblanc, J. Puebla, D. D. Solnyshkov, L. Klompmaker, I. A. Akimov, C. Louca, P. Muduli, A. Genco, M. Bayer, Y. Otani, G. Malpuech, A. I. Tartakovskii, *Nat. Photonics* **2022**, *16*, 632.
[21] S. Klembt, T. H. Harder, O. A. Egorov, K. Winkler, R. Ge, M. A. Bandres, M. Emmerling, L. Worschech, T. C. H. Liew, M. Segev, C. Schneider, S. Hofling, *Nature* **2018**, *562*, 552.
[22] L. Polimeno, G. Lerario, M. De Giorgi, L. De Marco, L. Dominici, F. Todisco, A. Coriolano, V. Ardizzone, M. Pugliese, C. T. Prontera, V. Maiorano, A. Moliterni, C. Giannini, V. Olieric, G. Gigli, D. Ballarini, Q. Xiong, A. Fieramosca, D. D. Solnyshkov, G. Malpuech, D. Sanvitto, *Nat. Nanotechnol.* **2021**, *16*, 1349.
[23] R. Suzuki, M. Sakano, Y. J. Zhang, R. Akashi, D. Morikawa, A. Harasawa, K. Yaji, K. Kuroda, K. Miyamoto, T. Okuda, K. Ishizaka, R. Arita, Y. Iwasa, *Nat. Nanotechnol.* **2014**, *9*, 611.
[24] N. Lundt, L. Dusanowski, E. Sedov, P. Stepanov, M. M. Glazov, S. Klembt, M. Klaas, J. Beierlein, Y. Qin, S. Tongay, M. Richard, A. V. Kavokin, S. Hofling, C. Schneider, *Nat. Nanotechnol.* **2019**, *14*, 770.
[25] Y.-J. Chen, J. D. Cain, T. K. Stanev, V. P. Dravid, N. P. Stern, *Nat. Photonics* **2017**, *11*, 431.
[26] J. Zhao, A. Fieramosca, R. Bao, W. Du, K. Dini, R. Su, J. Feng, Y. Luo, D. Sanvitto, T. C. H. Liew, Q. Xiong, *Nat. Nanotechnol.* **2022**, *17*, 396.
[27] M. S. Spencer, Y. Fu, A. P. Schlaus, D. Hwang, Y. Dai, M. D. Smith, D. R. Gamelin, X.-Y. Zhu, *Sci. Adv.* **2021**, *7*, eabj7667.
[28] W. Liu, Z. Ji, Y. Wang, G. Modi, M. Hwang, B. Zheng, V. J. Sorger, A. Pan, R. Agarwal, *Science* **2020**, *370*, 600.
[29] C. W. Hsu, B. Zhen, A. D. Stone, J. D. Joannopoulos, M. Soljačić, *Nat. Rev. Mater.* **2016**, *1*, 16048.
[30] B. Zhen, C. W. Hsu, L. Lu, A. D. Stone, M. Soljacic, *Phys. Rev. Lett.* **2014**, *113*, 257401.
[31] N. H. M. Dang, E. D. Simone Zanotti, C. Chevalier, G. Trippé-Allard, M. Amara, E. Deleporte, V. Ardizzone, D. Sanvitto, L. Claudio Andreani, C. Seassal, A. D. Gerace, H. S. Nguyen, *Adv. Opt. Mater.* **2022**, *10*, 2102386.
[32] A. M. Berghuis, G. W. Castellanos, S. Murai, J. L. Pura, D. R. Abujetas, E. van Heijst, M. Ramezani, J. A. Sanchez-Gil, J. G. Rivas, *Nano Lett.* **2023**, *23*, 5603.
[33] T. Weber, L. Kuhner, L. Sortino, A. Ben Mhenni, N. P. Wilson, J. Kuhne, J. J. Finley, S. A. Maier, A. Tittl, *Nat. Mater.* **2023**, *22*, 970.
[34] Y. Wang, J. Tian, M. Klein, G. Adamo, S. T. Ha, C. Soci, *Nano Lett.* **2023**, *23*, 4431.
[35] W. Liu, B. Wang, Y. Zhang, J. Wang, M. Zhao, F. Guan, X. Liu, L. Shi, J. Zi, *Phys. Rev. Lett.* **2019**, *123*, 116104.
[36] J. Tian, G. Adamo, H. Liu, M. Klein, S. Han, H. Liu, C. Soci, *Adv. Mater.* **2022**, *34*, 2109157.
[37] J. Wang, H. Li, Y. Ma, M. Zhao, W. Liu, B. Wang, S. Wu, X. Liu, L. Shi, T. Jiang, J. Zi, *Light: Sci. Appl.* **2020**, *9*, 148.
[38] K. Rong, B. Wang, A. Reuven, E. Maguid, B. Cohn, V. Kleiner, S. Katznelson, E. Koren, E. Hasman, *Nat. Nanotechnol.* **2020**, *15*, 927.

[39] E. I. Rashba, *Sov. Phys. Solid State* **1960**, *2*, 1109.
[40] K. Ishizaka, M. S. Bahramy, H. Murakawa, M. Sakano, T. Shimojima, T. Sonobe, K. Koizumi, S. Shin, H. Miyahara, A. Kimura, K. Miyamoto, T. Okuda, H. Namatame, M. Taniguchi, R. Arita, N. Nagaosa, K. Kobayashi, Y. Murakami, R. Kumai, Y. Kaneko, Y. Onose, Y. Tokura, *Nat. Mater.* **2011**, *10*, 521.
[41] N. Dahan, Y. Gorodetski, K. Frischwasser, V. Kleiner, E. Hasman, *Phys. Rev. Lett.* **2010**, *105*, 136402.
[42] S. Kim, B. H. Woo, S.-C. An, Y. Lim, I. C. Seo, D.-S. Kim, S. Yoo, Q. H. Park, Y. C. Jun, *Nano Lett.* **2021**, *21*, 10076.
[43] J. S. Swensen;, C. Soci, A. J. Heeger, *Appl. Phys. Lett.* **2005**, *87*, 253511.
[44] X. Y. Chin, D. Cortecchia, J. Yin, A. Bruno, C. Soci, *Nat. Commun.* **2015**, *6*, 7383.
[45] M. Klein, Y. Wang, J. Tian, S. T. Ha, R. Paniagua-Domínguez, A. I. Kuznetsov, G. Adamo, C. Soci, *Adv. Mater.* **2022**, *35*, 2207317.
[46] M. Klein, J. Li, A. Bruno, C. Soci, *Adv. Electron. Mater.* **2021**, *7*, 2100403.
[47] R. Su, A. Fieramosca, Q. Zhang, H. S. Nguyen, E. Deleporte, Z. Chen, D. Sanvitto, T. C. H. Liew, Q. Xiong, *Nat. Mater.* **2021**, *20*, 1315.
[48] R. Su, S. Ghosh, J. Wang, S. Liu, C. Diederichs, T. C. H. Liew, Q. Xiong, *Nat. Phys.* **2020**, *16*, 301.
[49] R. Su, S. Ghosh, T. C. H. Liew, Q. Xiong, *Sci. Adv.* **2021**, *7*, eabf8049.
[50] D. Shi, V. Adinolfi, R. Comin, M. Yuan, E. Alarousu, A. Buin, Y. Chen, S. Hoogland, A. Rothenberger, K. J. S. Katsiev, *Science* **2015**, *347*, 519.
[51] S. Makarov, A. Furasova, E. Tiguntseva, A. Hemmetter, A. Berestennikov, A. Pushkarev, A. Zakhidov, Y. Kivshar, *Adv. Opt. Mater.* **2019**, *7*, 1800784.
[52] C. Soci, G. Adamo, D. Cortecchia, K. Wang, S. Xiao, Q. Song, A. L. Schall-Giesecke, P. J. Cegielski, M. C. Lemme, D. Gerace, D. Sanvitto, J. Tian, P. A. Tonkaev, S. V. Makarov, Y. S. Kivshar, O. A. Jimenez Gordillo, A. Melloni, A. P. Pushkarev, M. D'Amato, E. Lhuillier, A. Bramati, *Opt. Mater. X* **2023**, *17*.
[53] Y. Jiang, A. M. Soufiani, A. Gentle, F. Huang, A. Ho-Baillie, M. A. Green, *Appl. Phys. Lett.* **2016**, *108*, 061905.
[54] T. Yoda, M. Notomi, *Phys. Rev. Lett.* **2020**, *125*, 053902.
[55] R. Mermet-Lyaudoz, F. Dubois, N.-V. Hoang, E. Drouard, L. Berguiga, C. Seassal, X. Letartre, P. Viktorovitch, H. S. Nguyen, arXiv:1905.03868 **2019**.
[56] Y. Chen, H. Deng, X. Sha, W. Chen, R. Wang, Y. H. Chen, D. Wu, J. Chu, Y. S. Kivshar, S. Xiao, C. W. Qiu, *Nature* **2023**, *613*, 474.
[57] X. Zhang, Y. Liu, J. Han, Y. Kivshar, Q. Song, *Science* **2022**, *377*, 1215.
[58] L. Zhang, R. Gogna, W. Burg, E. Tutuc, H. Deng, *Nat. Commun.* **2018**, *9*, 713.
[59] F. Maddalena, X. Y. Chin, D. Cortecchia, A. Bruno, C. Soci, *ACS Appl. Mater. Interfaces* **2018**, *10*, 37316.
[60] Y. Wang, A. Giorgio, H. Son Tung, T. Jingyi, S. Cesare, **2024**, https://doi.org/10.21979/N9/EGB3GG.